Ceramics International 48 (2022) 37433–37447

Contents lists available at ScienceDirect

Ceramics International

journal homepage: www.elsevier.com/locate/ceramint

Final surface modification for better wear resistance of ceramic coating on cast AlSi10Mg alloy

Roman Gabor [a,*], Tomáš Prymus [a], Ladislav Cvrček [b], Václav Nehasil [c], Josef Hlinka [d,e], Matěj Buřil [b], Michaela Tokarčíková [a], Jana Seidlerová [a,f]

[a] Nanotechnology Centre, CEET, VSB – Technical University of Ostrava, 17. Listopadu 15/2172, 708 00, Ostrava-Poruba, Czech Republic
[b] Department of Materials Engineering, Faculty of Mechanical Engineering, Czech Technical University in Prague, Karlovo Náměstí 293/13, 120 00, Prague 2, Czech Republic
[c] Department of Surface and Plasma Science, Charles University, Prague, Czech Republic
[d] Department of Materials Engineering and Recycling, Faculty of Materials and Technology, VŠB-Technical University of Ostrava, 17. Listopadu 2172/15, 708 00, Ostrava-Poruba, Czech Republic
[e] Centre for Advanced Innovation Technologies, VSB-Technical University of Ostrava, 17. Listopadu 2172/15, 708 00, Ostrava-Poruba, Czech Republic
[f] Department of Chemistry and Physico-Chemical Processes, Faculty of Materials and Technology, VŠB-Technical University of Ostrava, 17. Listopadu 2172/15, 708 00, Ostrava-Poruba, Czech Republic

ARTICLE INFO

Keywords:
Micro-arc oxidation
Design of experiment
Coating
Wear
Al–Si alloys

ABSTRACT

Using the design of experiment (DOE) method and the micro-arc oxidation (MAO) technique, ceramic layers on AlSi10Mg alloy were systematically prepared to design optimal process conditions for achieving the best tribological properties of the ceramic layers. The lowest concentrations of the applied 6 g/l NaOH and 12 g/l Na_2SiO_3 resulted in the preparation of uniform MAO layers with the lowest rated parameters R_a, R_z and thickness achieved under micro-arc discharge conditions at 500 V and 60 min. With the increasing thickness of the coatings, there was an increase of Si in the MAO coating. Full factorial DOE was used to optimize the tribological properties in a polyalphaolefin (PAO) environment at 80 °C. The most significant influence for the preparation of abrasion-resistant layers for the investigated factors was identified on the AlSi10Mg alloy by the NaOH content in the electrolyte. The friction coefficients of MAO coatings reached an average value of 0.15. Aero-lap polishing technology was applied for increased wear resistance requirements to eliminate the deficiencies of MAO coatings, leading to decrease wear track by almost double compared to polished silumin. Removal of the outer MAO layer by polishing led to a reduction in the high corrosion resistance of the MAO coating, demonstrating the influence of the outer layer not only on the tribological properties but also on the corrosion resistance of MAO coatings.

1. Introduction

Al–Si alloys are one of the most important aluminium-based foundry alloys, commonly used in automotive and aerospace industries due to their excellent properties such as castability, strength-to-weight ratio and good thermal and electrical conductivity. As a result, Al–Si alloys are finding more applications in the mentioned sectors, particularly in the manufacturing of cylinders, pistons, engine blocks and brake callipers [1–3].

Due to the requirements of the producers of individual products for the long-term durability of castings, the application of Al–Si alloys is significantly limited due to low corrosion resistance and surface hardness [4]. In order to improve the abrasion and corrosion resistance of Al–Si alloys, their surfaces are modified using anodic oxidation of the substrate [5–7] or the relatively newly developed method of thermal spraying [8,9].

The widespread implementation of convex hard anodization for surface treatment of AlSi10Mg alloys is limited by the microstructure of the alloy, which is formed by α(Al) dendrites in addition to the primary α(Al) dendrites and α(Al)+Si eutectic [10]. The resulting oxide layers prepared by hard anodization do not have sufficient abrasion and corrosion resistance. Therefore the possibility of using the relatively new technique of micro-arc oxidation (MAO) arises for the surface treatment of Al–Si alloys which has been verified in several works [11–13]. This

* Corresponding author.
E-mail address: roman.gabor@vsb.cz (R. Gabor).

https://doi.org/10.1016/j.ceramint.2022.09.224
Received 21 July 2022; Received in revised form 16 September 2022; Accepted 18 September 2022
Available online 21 September 2022

Table 1
Chemical composition AlSi10Mg.

Sample	Element (wt. %)								
	Si	Fe	Cu	Mn	Mg	Ni	Zn	Pb	Ti
AlSi10Mg	10.0	0.33	0.21	0.03	0.26	0.01	0.07	0.01	0.08

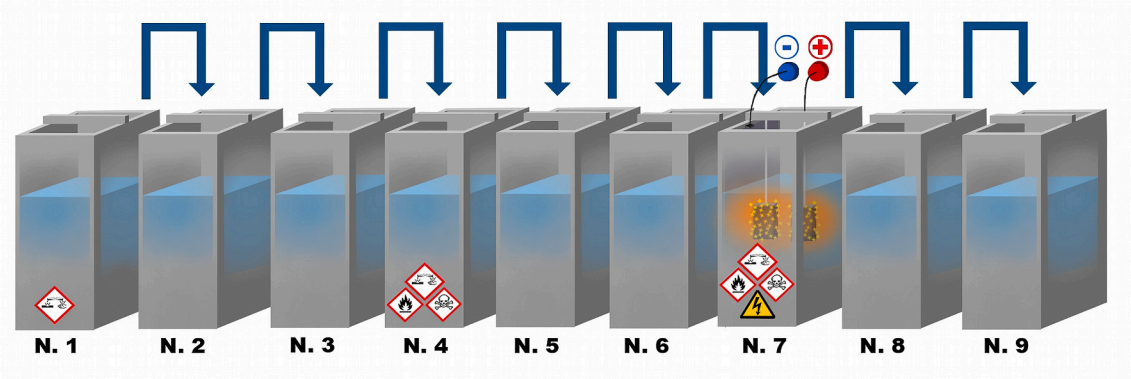

Fig. 1. MAO process.

technique is used to prepare a ceramic adhesion coating with a compact corrosion-resistant and abrasion-resistant inner layer and an outer porous layer under elevated stress conditions to produce a dielectric discharge [14].

Key parameters for the preparation of MAO layers include the choice of electrolyte, which significantly affects the growth mechanism of the oxide layer and its corrosion and mechanical properties [15]. The most commonly used electrolytes for the preparation of the oxide layer in Al–Si alloys include silicon-containing electrolytes [16–18]. However, the presence of eutectic and silicate ions in the electrolyte influences the resulting topography of the oxide layer due to the emergence of "craters" on the surface of the coating representing rapidly solidified melt of the oxidized substrate flowing through discharge channels to the surface [19]. This leads to deterioration of the tribological properties and an increase of the coefficient of friction leading to a significant limitation in the use of MAO coatings for Al–Si alloys and their application in the field of lubricated engine components. As a result, increased attention has been paid to the development of self-lubricating MAO coatings based on Al_2O_3/PTFE composite coating [20], multiphase MAO coating containing graphite [21], Si_3N_4/TiO_2 nanocomposite coating [22], or synthesized MoS_2 layer on the surface of MAO coating [23]. However, an optimal, economically feasible procedure is still being sought to enable the efficient preparation of MAO coating, meeting the requirements for broader Al–Si applications in terms of tribological and corrosion resistance properties. To this end, statistical analysis methods such as the systematic design of experiment (DOE) approach are used to optimize and describe the individual input factors' influence [24].

This article presents a procedure for the preparation of abrasion and corrosion-resistant MAO coating using DOE. Main results of this work are (1) determination of the optimum process conditions of the MAO process including the importance of the main factors influencing the tribological behaviour of the coating in polyalphaolefin (PAO) at 80 °C, (2) description of the application procedures of Aero-lap polishing to improve the tribological properties of MAO coatings, (3) evaluation of the tribological and corrosion properties of the outer and inner layer of MAO coatings. The results indicate the potential application of the above-mentioned technique in the field of lubricated motor components made of Al–Si alloy requiring high wear and corrosion resistance.

2. Experimental

2.1. Materials and sample preparation

Surfaces of AlSi10Mg foundry alloy samples (20 mm (L)*10 mm (W)*5 mm (H)) were treated by tumbling in HV 20 tube vibrator (OTEC, Germany) to homogenise them. Steel satellites (5 × 3 mm) were used as process media for 24 h, followed by 72 h of lapping in plastic grinding chips M 10. The lapping procedures were carried out under wet conditions. Finally, the alloy was digested in an acid mixture in a Milestone Ethos Up microwave digestion plant (Italy). Selected elements (Table 1) were determined by atomic emission spectroscopy with inductively coupled plasma (AES-ICP, Spectro Arcoss, Germany).

2.2. Surface modification process

The MAO coating preparation was performed according to the combination based on the DOE on the semi-operational unit shown in Fig. 1. The switching power supply (DEHOR-spec. Litvínov s.r.o., Czech Republic) with a pulse unit was controlled by a constant voltage of 500 V for 60 min. The MAO process was carried out with the sample as anode and a stainless steel sheet (1.4301) of 2 mm thickness serving as a cathode. The electrolyte composition was defined by the designed DOE with temperature controlled up to 25 °C during the MAO process.

N. 1) Mixed degreasing bath (1 M NaOH; 45 °C); **N. 2,3**) Mixed rinsing bath (distilled water; conductivity <10 μS/cm); **N. 4)** Pickling bath (20 wt % HNO_3+2 wt % HF); **N. 5,6)** Mixed rinsing bath (distilled water; conductivity <10 μS/cm); **N. 7)** Mixed rinsing electrolyte bath with counter - electrode (electrolyte; pH ≥ 12). **N. 8,9)** Mixed rinsing bath (distilled water; conductivity <10 μS/cm).

To improve the tribological properties, a lapping technique was applied to the optimal DOE experiment using an aero-lap polishing machine (AERO LAP YT300-OE, Japan). Verification of the tribological properties improvement was carried out at 1, 2 and 3 min time, working pressure 0.7 MPa, working distance 100 mm, and rubber granules (Multicon) of size 0.5–2 mm with diamond paste as process media.

2.3. Design of experiment (DOE)

The design of experiments, including the selection of factors and their limit values, was based on the empirical experience of the authors.

Table 2
Levels main factors.

Parameters	Factor	Low level (−1)	High level (+1)
A	NaOH (g/l)	6	12
B	Na_2SiO_3 (g/l)	9	18
C	Frequency (Hz)	95	130

Table 3
Full factorial design.

Test	NaOH (g/l)	Na_2SiO_3 (g/l)	Frequency (Hz)
1	6	12	130
2	9	12	130
3	6	18	130
4	9	18	130
5	6	12	95
6	9	12	95
7	6	18	95
8	9	18	95

Selected three main factors were tested for their influence on the resulting tribological properties in two levels (2^3 factorial design). The selected limit values of each factor (see Table 2) were applied with repetition without central points. The full factorial design, including the combination of the levels of each factor, is shown in Table 3.

2.4. Surface characterisation

Surface and cross-section images of the samples were taken using a JEOL JSM-7610F Plus scanning electron microscope (JEOL, Japan) in secondary (SE) and backscattered electron (BSE) mode. The chemical composition of MAO coatings and elemental mapping were studied using a dispersive X-ray spectrometer (EDS, ULTIM MAX 65 mm^2, Oxford Instruments, England) attached to the SEM. The surface morphology of the samples was evaluated further using correlative analysis providing data from AFM LiteScopeTM (Nenovision s.r.o., Czech Republic) and SEM allows 3D-CPEM view (Correlative Probe and Electron Microscopy), optical 3D IF-SensorR25 instrument (Bruker Alicona, Austria), profilometer Talysurf 50 (Taylor Hobson, England).

Analysis of elements and their chemical states was performed by X-ray photoelectron spectroscopy (XPS) in a UHV chamber with a base pressure of around $3{\cdot}10^{-7}$ Pa. The measurement system consists of an Omicron EA 125 multi-channel analyser and a dual anode (Mg/Al) X-ray source. The primary energy source was the Al Kα line (1486.6 eV). The measurement system was calibrated against the binding energy of C1s (284.5 eV).

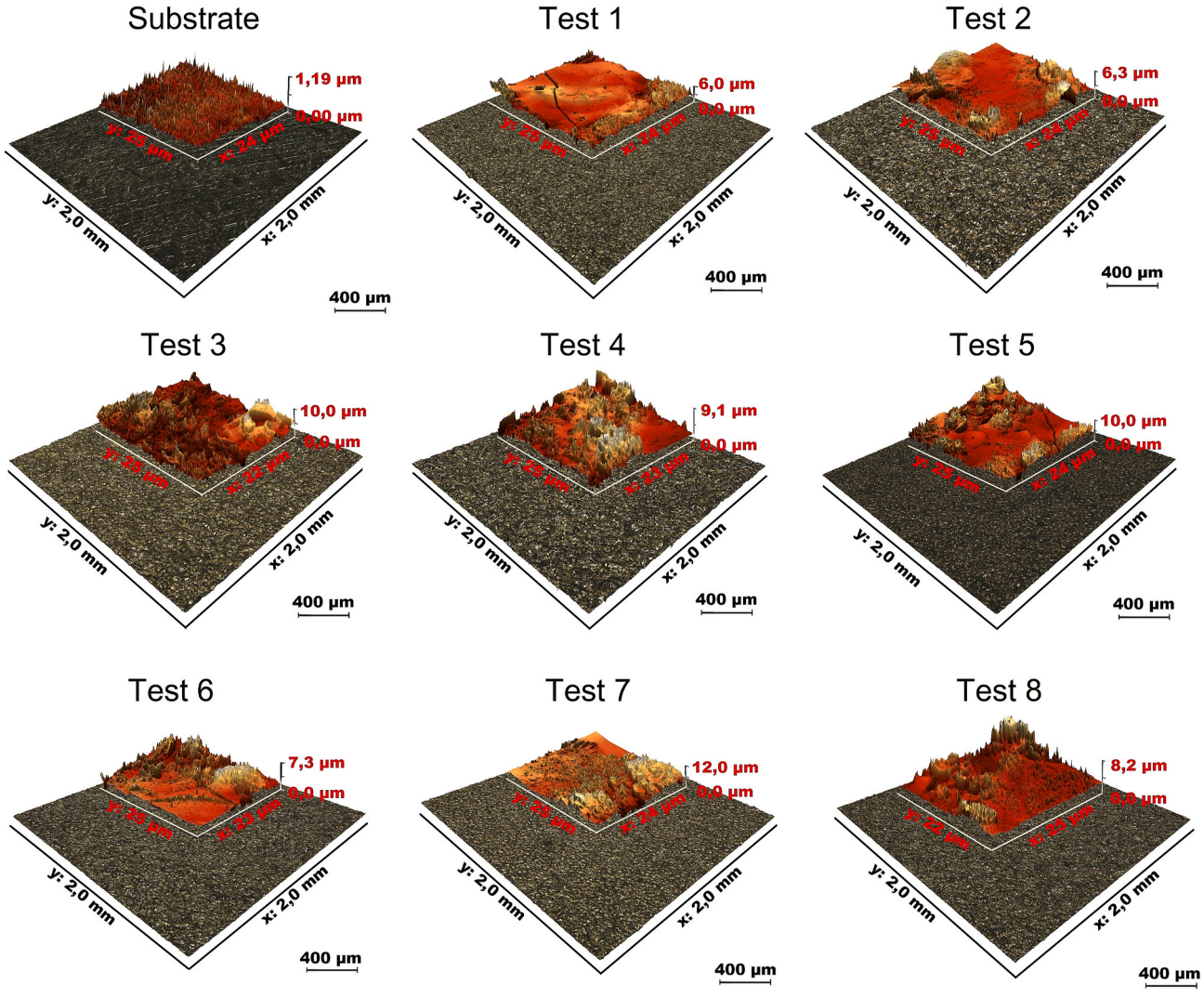

Fig. 2. Optical images with 3D-CPEM.

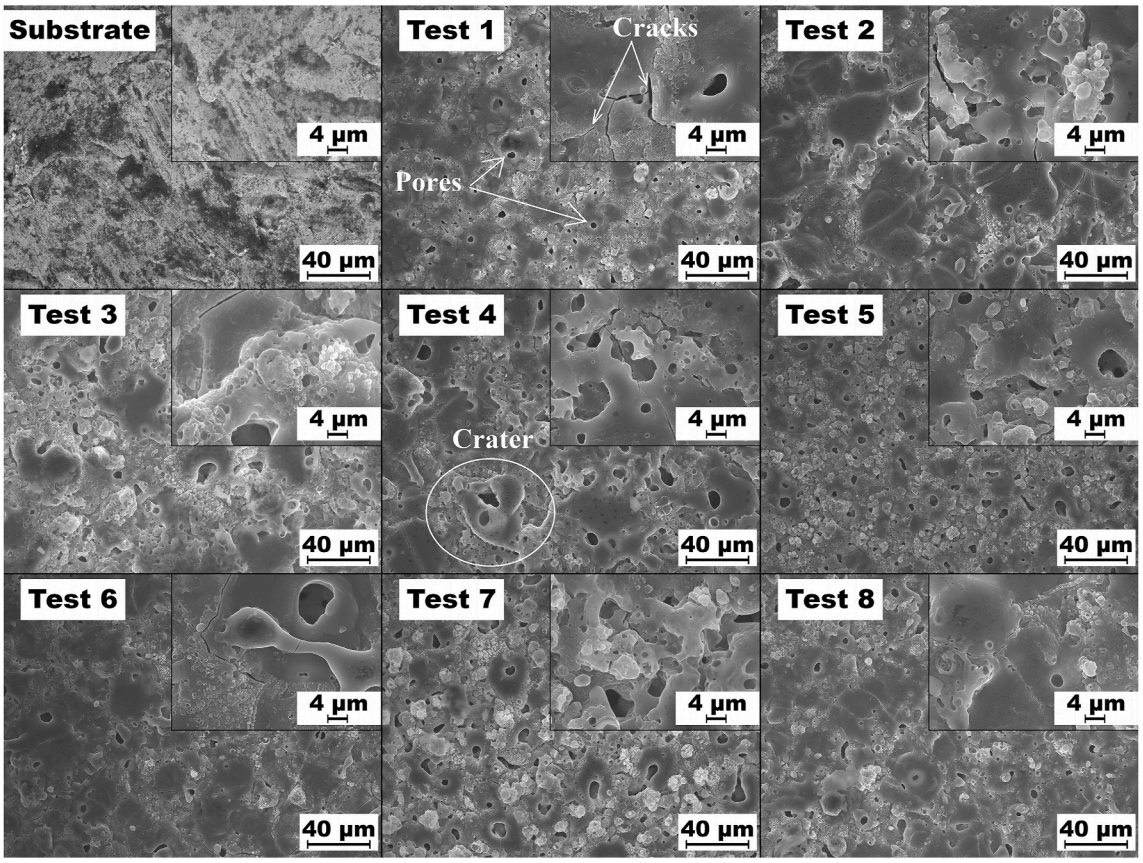

Fig. 3. SEM images of MAO coatings.

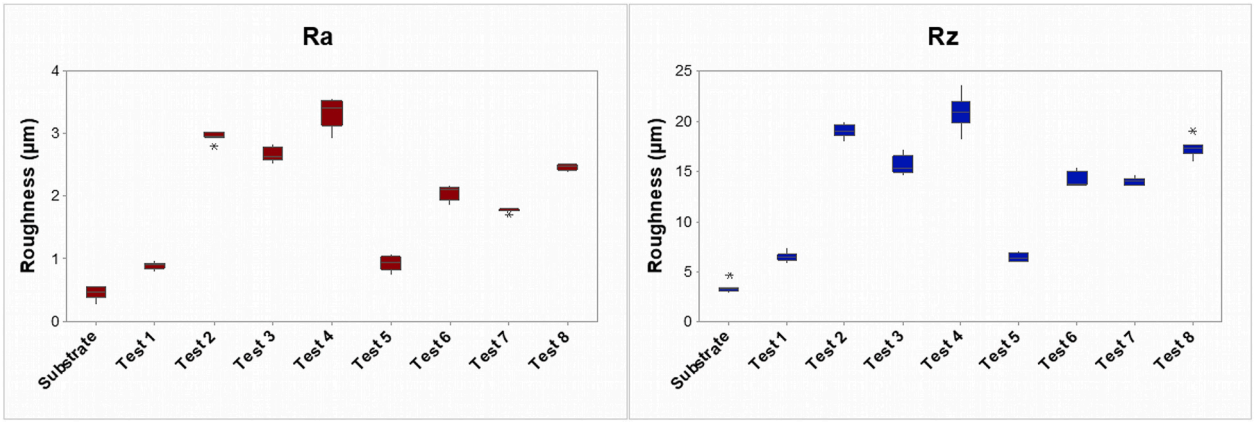

Fig. 4. Surface roughness of MAO coatings: Parameters R_a, R_z.

2.5. Tribological tests

A ball-on-disk CSM THT tribometer (CSM Instruments, Switzerland) was used to determine the tribological properties. The friction pair consisted of the MAO coating on a planar sample and an Al_2O_3 ball 6 mm in diameter. Polyalphaolefin (PAO) liquid was chosen as the test environment. PAO is a non-polar synthetic hydrocarbon liquid that is the main synthetic base component of most oils used in industrial and automotive lubricants. PAO provide superior lubrication performance over a wider operating temperature range than petroleum oils and is less volatile.

Specifically, PAO Labovac 14 (Welch, Germany) was chosen as a suitable reference for tribological measurements. The manufacturer states a viscosity index of 29.0 mm^2/s at 40 °C and 5.6 mm^2/s at 100 °C. Since the viscosity index decreases significantly with increasing temperature, tribological tests were performed at a temperature of 80 °C to ideally simulate typical engine operating temperatures.

Measurements were performed twice at a normal load of 2 N, a number of laps 10000, linear sliding speed 50 mm/s and a radius of 4 mm. The friction coefficient (μ) was calculated from the ratio of the tangential friction force and the normal force. The width of the wear track was evaluated using a digital microscope Olympus DSX1000 (Olympus Corporation, Japan).

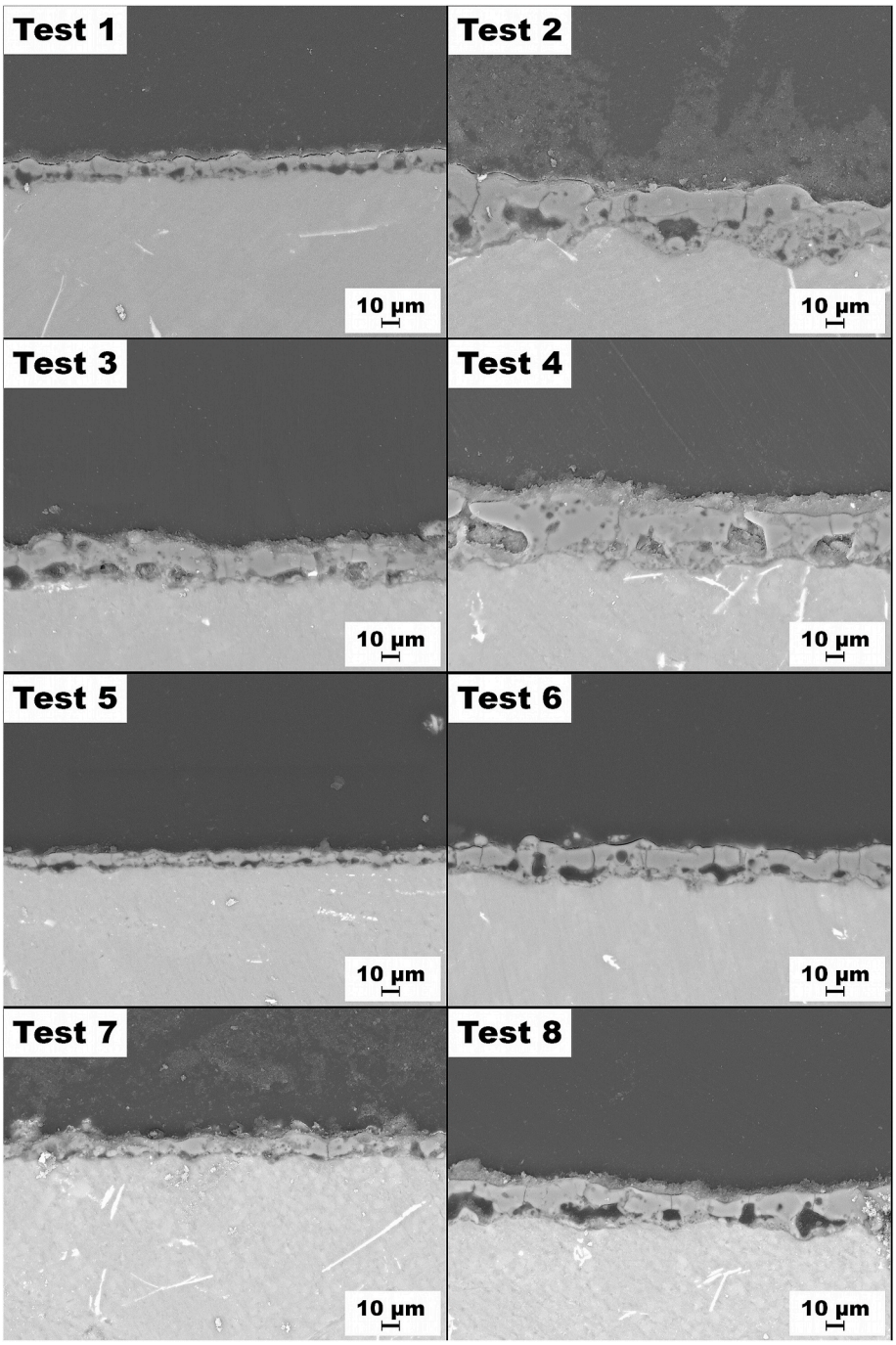

Fig. 5. Cross section of MAO samples.

2.6. Adhesion tests

The CSM Revetest Xpress + device (CSM Instruments, Switzerland) was used for the scratch test. The scratch tester equipped with a Rockwell diamond indenter (tip radius 200 µm) was used. The scratch test load was set to linearly increase from 1 N to 50 N along the 5 mm scratch path and linear speed 10 mm/min.

2.7. Corrosion tests

Samples were exposed to neutral salt spray using a corrosion chamber SKB 400 A-TR (Gebr. Liebisch GmbH, Germany) according to ČSN EN ISO 9227 for 300 h. The concentration of the sprayed NaCl solution was 50 ± 5 g/l. The average pH of the accumulated saline solution was 7.0. The samples were stored in the corrosion chamber at an inclination of 20° ± 5°.

The samples were further tested in a three-electrode system (Voltalab PGZ 100, SAS OrigaLys ElectroChem, France). The sample was connected as a working electrode; the calomel electrode was used as a reflection electrode, and the carbon rod as an auxiliary electrode. Potentiodynamic polarisation tests were performed in a 3.5 wt % NaCl solution over a sample area of 0.5 cm^2. The initial potential of the potentiodynamic measurements was set to −150 mV vs open circuit potential (OCP) after stabilisation of the corrosion equilibrium with a polarisation rate of 5 mV/s.

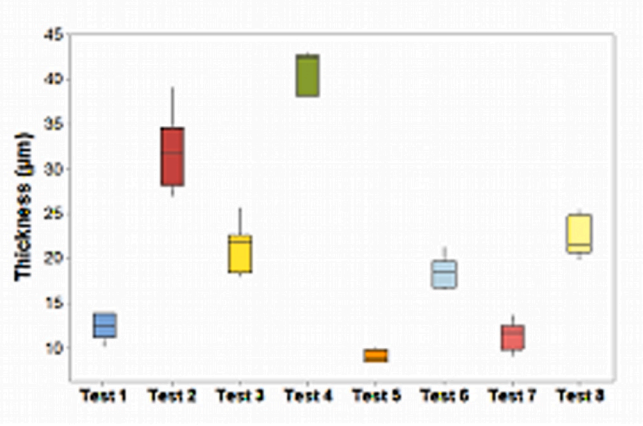

Fig. 6. Thickness MAO coatings.

Table 4
Chemical analysis of surfaces by EDX.

Test	wt. %		
	O	Al	Si
1	41.87 ± 0.34	39.45 ± 0.28	18.68 ± 0.23
2	39.37 ± 0.37	33.08 ± 0.26	27.55 ± 0.27
3	45.55 ± 0.35	17.42 ± 0.19	37.03 ± 0.28
4	40.90 ± 0.37	26.60 ± 0.24	32.51 ± 0.28
5	39.92 ± 0.34	35.14 ± 0.25	24.94 ± 0.24
6	38.48 ± 0.38	39.09 ± 0.29	22.43 ± 0.25
7	42.29 ± 0.38	21.09 ± 0.22	36.62 ± 0.30
8	38.89 ± 0.35	33.22 ± 0.25	27.89 ± 0.25

2.8. Statistical analyses

Data related to surface morphology for each test were compared with each other using One-way ANOVA followed by the Tukey test. The statistical analyses were carried out using Minitab® 17 statistical software. Results were presented as mean ± standard deviation (S.D.). Differences between tests were evaluated at a statistical significance $p < 0.01$.

3. Results and discussion

3.1. Surface topography of MAO coatings

Different morphology of the input ground surface of the substrates and oxide layers prepared using different process conditions were observed in Fig. 2 (Table 3) using optical imaging and correlative CPEM analysis.

The substrate surfaces of each test (shown in Fig. 3) were analysed with SEM, which confirmed the presence of micro-defects of MAO coatings. The evolution of the coating (following the reaching of the dielectric discharge) is accompanied – besides the structural changes – by the formation of so-called volcanic craters (Fig. 3, Test 4). These structures are formed in the presence of micro-discharge to form melt that flows out through so-called discharge channels towards the surface, where it is rapidly cooled in the electrolyte environment. Areas with a surface microstructure exhibit a greater presence of these craters and directly affect the resulting roughness of MAO surfaces [25]. During the MAO process, gas development occurs; the gas passes through the microchannels and, together with the solidifying melt, forms a porous structure with localised microcracks (Fig. 3, Test 1). The intensity of the internal stresses released by the coating corresponds to the micro-arc discharge conditions with subsequent rapid cooling in the electrolyte environment under the individual DOE tests [26].

Surface roughness was evaluated using the parameters R_a (average roughness of surface), R_z (average of the absolute values of the heights and depths) and their resulting values were compared for each DOE test using one-way analysis of variance (ANOVA). The results of the relative positions of the observed groups of parameters R_a, R_z are shown in Fig. 4. The results confirm the statistically significant effect of the DOE parameters on the roughness of the surfaces when the null hypothesis is rejected ($p < 0.01$), where at least one mean of the R_a and R_z parameters is statistically different. The statistical agreement was demonstrated for the parameters R_a, R_z for tests 5 and 1. In the case of the R_z surface parameter, tests 6 and 3, as well as tests 7 and 6 were found to be statistically indistinguishable. The surface parameter R_a was similar for tests 8 and 3. In several studies [27,28], the influence of silicate content on the resulting surface roughness was confirmed. The DOE experiment confirmed the effect of NaOH addition and the presence of silicates on the resulting roughness (Fig. 4). As both the concentration of NaOH, Na_2SiO_3 and the conductivity of the electrolyte increases, there was a stronger micro-arc discharge observed, more melt transfer towards the surface and an increasing representation of the so-called craters on the sample surfaces, which in turn affected the resulting surface roughness. Using the lowest NaOH, Na_2SiO_3 contents (Test 1, 5) of the selected DOE combinations, uniform surfaces with the lowest evaluated parameters R_a, R_z were achieved without any observed effect of the applied source frequency. The resulting quality of the surfaces, in terms of the frequency of microdefects, is crucial for the corrosion and tribological properties of the surfaces.

3.2. Cross section and chemical composition

During the MAO process (60 min at 500 V), an increase in the oxide layer (Fig. 5) was observed, accompanied by a decrease in current. Different oxide layer thicknesses were obtained by combining the parameters based on the DOE design. The results presented in Fig. 6 confirm the influence of the chosen parameters on the resulting coating thickness and, thus, lead to the rejection of the null hypothesis ($p < 0.01$) that all diameters are equal. The use of one-way Analysis of Variance (ANOVA) also confirmed that – based on the comparison of the individual tests – the averages of the 5-1, 6-3, and 8-3 tests are statistically indistinguishable ($p > 0.01$). The smallest thicknesses were achieved at the lowest concentrations of NaOH and Na_2SiO_3 used; the effect of the frequency used was not evident in the case of the smallest layer thickness. On the contrary, the greatest thickness was obtained when the electrolyte had the highest NaOH and Na_2SiO_3 content and when the frequency used was 130 Hz. These results correspond with the observed roughness parameters and can be explained based on the mechanism of MAO layer formation [29]. As the ionic content of the solution increases, a more intense discharge occurs, accompanied by a linear increase in the layer thickness due to a larger volume of melt passing through the discharge channels depositing on the cooled oxide surface with an increasing proportion of craters and pores.

The elemental composition of the MAO coatings shown in Table 4 was studied using EDX at 50x magnification due to the presence of the eutectic α(Al)+Si and the inhomogeneity of the coatings. The increased Si contents correspond to tests with higher Na_2SiO_3 content in the electrolyte; the elemental distribution of the resulting Al–O–Si system (Fig. 7) confirms the presence of Si in the layer. According to Chao et al. [30], silicon is mainly incorporated in the outer layer of the coating during the MAO process from electrophoresis and diffusion of the present SiO_3^{2-} from the electrolyte. During the MAO process, several reactions occur at the anode, leading to the formation of a complex Al–Si–O system under plasma discharge conditions (>3500 K) [31–33].

$$2OH^- - 2e^- \rightarrow H_2O + 1/2O_2 \quad (1)$$

$$Al \rightarrow Al^{3+} + 3e^- \quad (2)$$

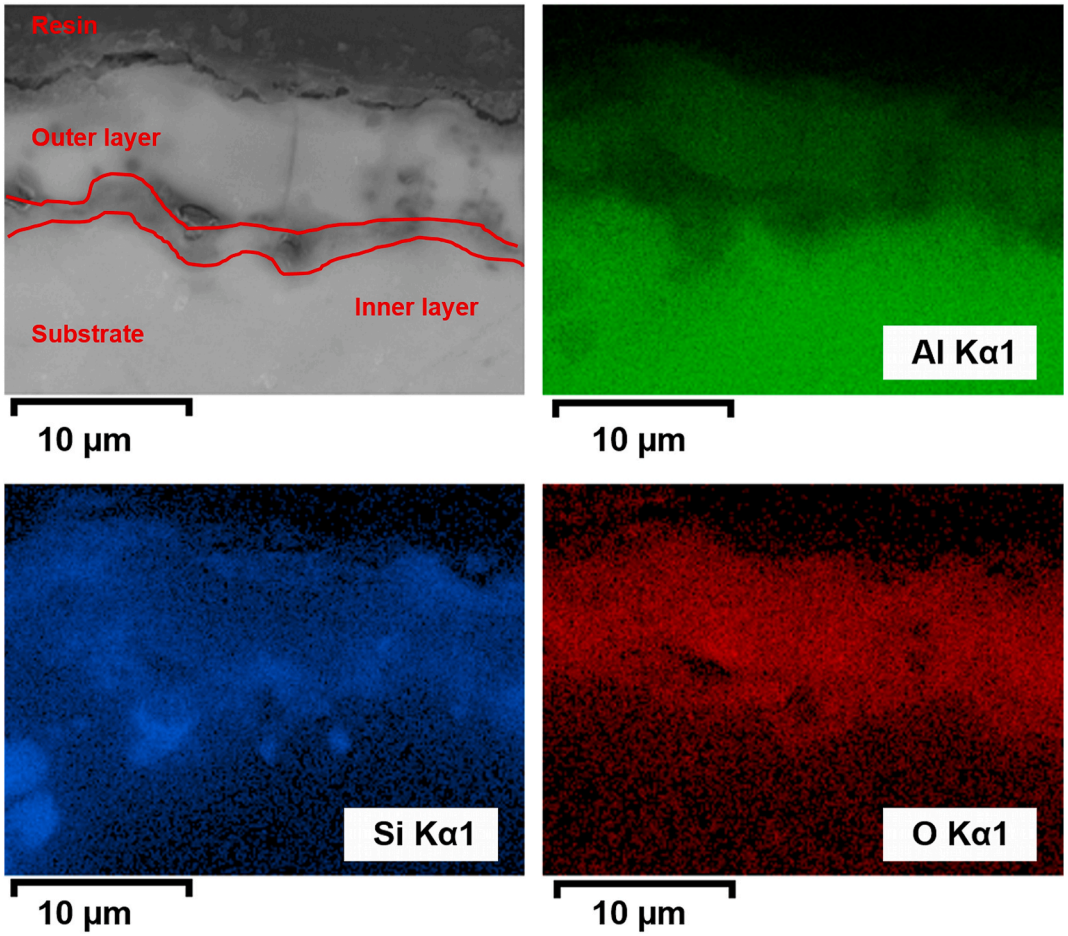

Fig. 7. SEM/EDX mapping images of MAO coatings.

$$2Al^{3+} + 3O^{2-} \rightarrow Al_2O_3 + 6e^- \quad (3)$$

$$SiO_3^{2-} - 4e^- \rightarrow 2SiO_2 + O_2 \quad (4)$$

$$ySiO_2 + xAl_2O_3 \rightarrow ySiO_2.xAl_2O_3 \quad (5)$$

The results of the XPS analysis of the chemical states of the crucial elements (C, Al, Si, O) present on the surface of the layers are shown in Fig. 8. All binding energies were calibrated to the main C 1s peak (284.5 eV). The presence of carbon can be explained by the presence of graphitic carbon admixture due to the width of the determined peak. The Si 2p binding energy (103.8 ± 0.2 eV) corresponds to the presence of SiO_2, which is formed during the MAO process from silicates present in the electrolyte (Eq. (4)). The Al 2p line (75.4 eV) in the spectrum indicates the presence of an oxide phase. A shift to higher values of about 1 eV compared to the tabulated value for Al_2O_3 indicates the probable presence of the aluminosilicate (Eq. (5)) [34]. The O 1s peak (530.6 ± 0.1 eV) is in the range of binding energies that correspond to the presence of an oxide phase [35].

3.3. Tribological properties of MAO coatings in oil

The decisive parameter for selecting the most suitable type of MAO layer was the evaluation of its wear. The combination of a hard and brittle MAO layer on a tough silumin base material can be sensitive to the initial point pressure during running-in. Therefore, the tests were performed in PAO oil to make the running-in phase as gentle as possible. At the same time, a small 2 N load, a standard linear sliding speed of 50 mm/s, a radius of 4 mm, and 10000 cycles (corresponds to the track 251 m) were used. Fig. 9a shows a comparison of the friction coefficients of the MAO layers (Test 1–8), where the friction counterpart was an Al_2O_3 ball. The MAO layers showed relatively high porosity (Fig. 3) and roughness (Fig. 4). In some cases, abrasive particles formed during the running-in phase, which caused an unstable course of friction. The exception was Test 5 layer, which behaved very stably, and its coefficient of friction was also the lowest of all tested MAO layers. However, it was still higher than that of pure silumin, which served as a reference sample. In this case, however, it was a polished surface. Fernández-López et al. [12] reported a similar course of the friction coefficient for silumin with and without MAO treatment with a polished surface.

The situation was similar in the case of the wear track width evaluation. It can be seen in Fig. 9b that the Test 5 sample had the smallest track width and slight abrasive wear of the ball (Fig. 10a). Additionally, the thickness of the Test 5 layer was the lowest of all the layers (Fig. 6), and its abrasion should manifest itself much earlier than the other layers. However, it must be noted that the track width was only slightly smaller than that of polished silumin (Fig. 9b), where adhesive friction predominated between the ball and the sample (Fig. 10c). For a precise determination, it would be necessary to compare samples with similar surface roughness. On the contrary, the Test 8 sample showed the greatest wear track, where abrasive friction prevailed between the ball and the sample (Fig. 10b).

3.4. Adhesion of MAO coating

The scratch test method was used to compare the adhesion of the MAO coatings. A linearly increasing load was set for testing from 1 N to 50 N. The load was chosen so that the resulting scratch depth was

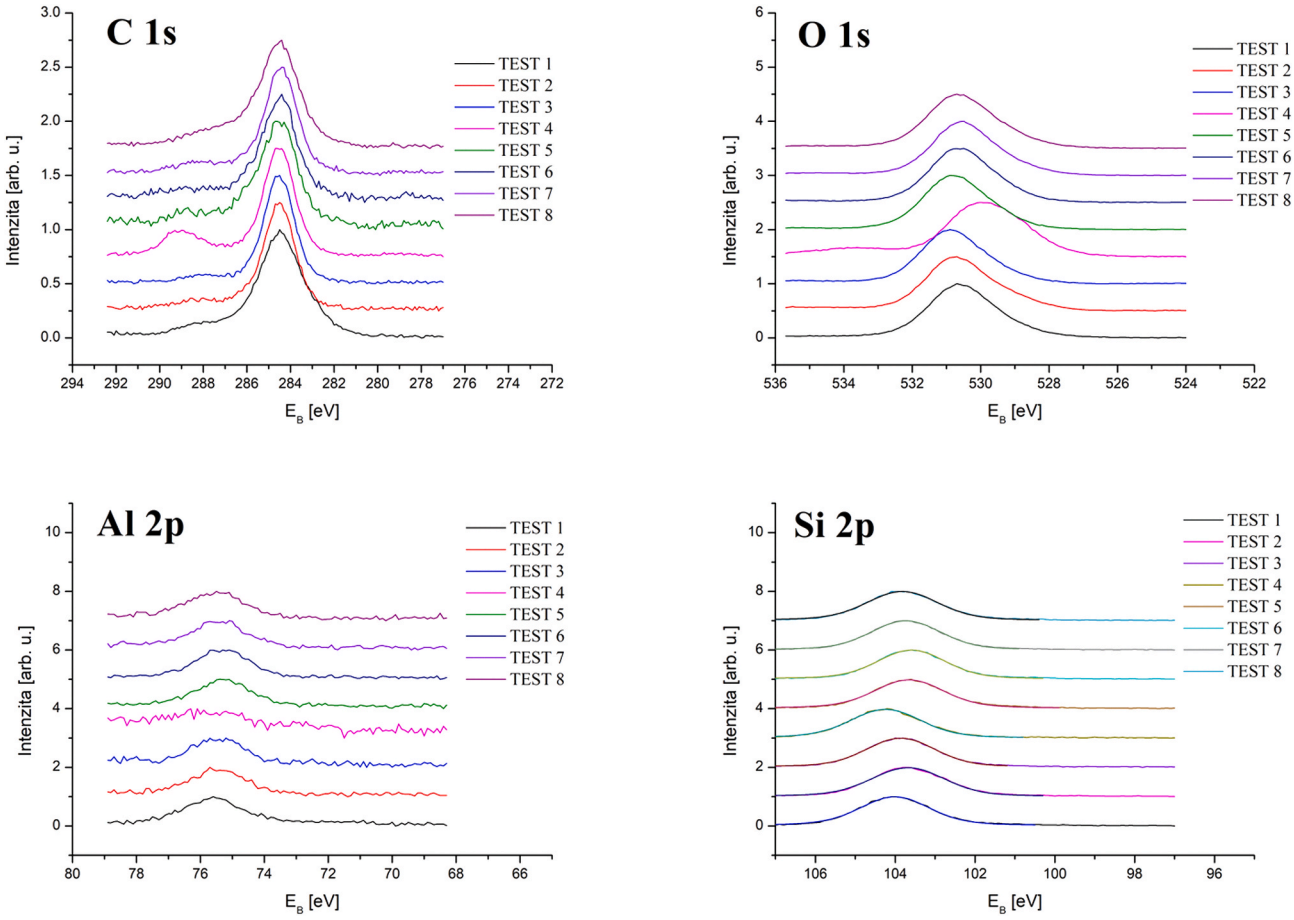

Fig. 8. XPS spectrum of MAO coatings.

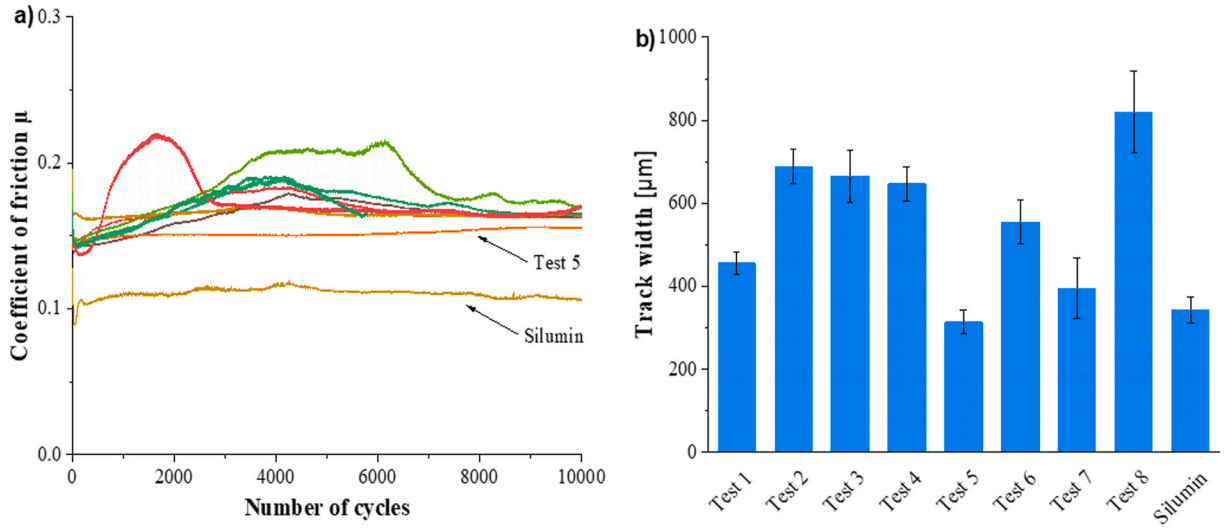

Fig. 9. Comparison of a) the friction coefficients and b) the wear tracks of the MAO layers Test 1–8. Polished silumin was used as a reference.

comparable to the scratch depth in the standard scratch test, where the hard base material and load up to 100 N are used.

The tests performed did not show failures in the cohesion or adhesion of the MAO coatings. This is consistent with the growth mechanism of MAO coatings, which are formed by surface oxidation and form a compact system with the base material. The porosity of the MAO coatings varied greatly, as confirmed in Fig. 3. More porous MAO coatings could have formed abrasive particles to a greater extent and increased wear. This assumption was verified in MAO coatings with the lowest and highest wear. Fig. 11 compares the scratches of the samples with the highest wear resistance (Test 5) and the lowest wear resistance (Test 8). There was no damage to the cohesion or adhesion of the MAO coatings around the scratches. Therefore, the degradation of the wear resistance of the Test 8 sample is not caused by adhesion failure, but by the

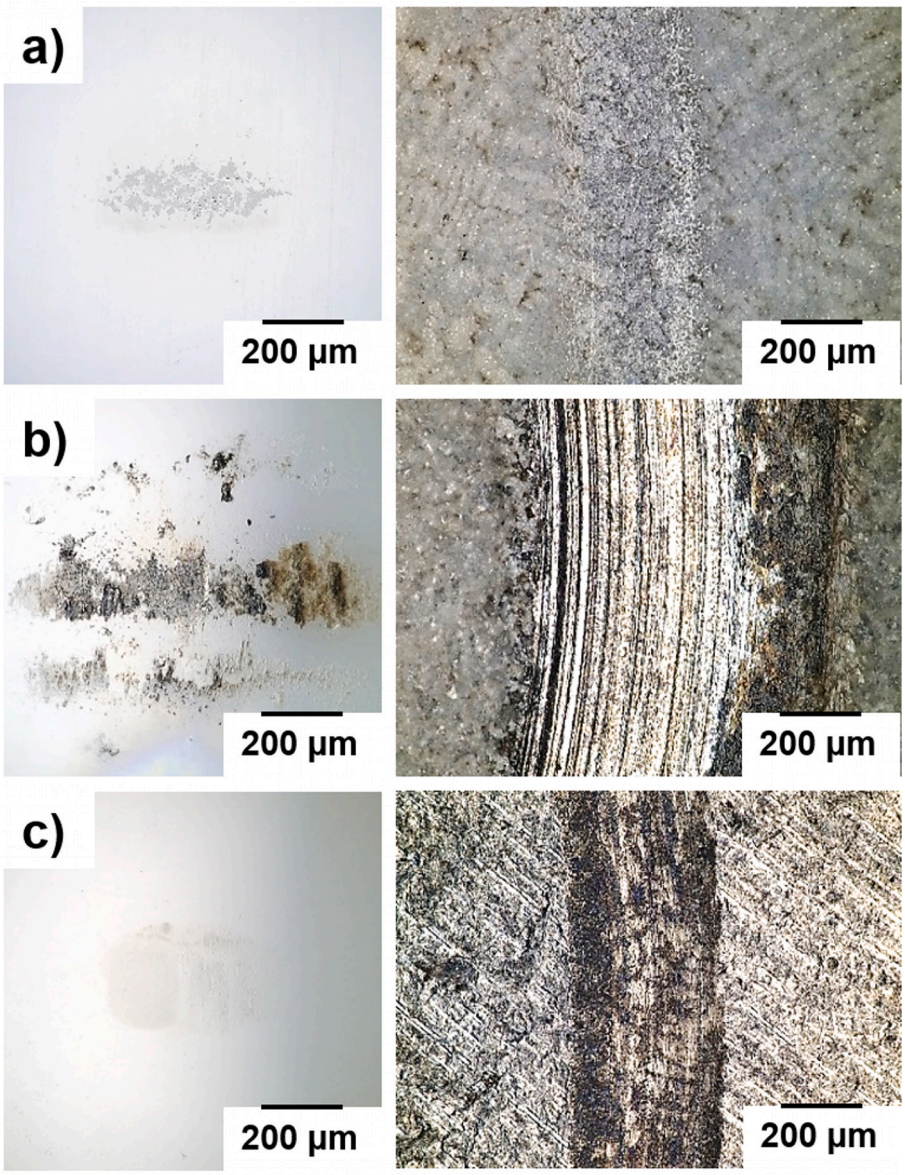

Fig. 10. Comparison of the wear of the Al_2O_3 ball (left) and the wear track of sample (right) for: a) Test 5 sample, b) Test 8 sample, and c) silumin.

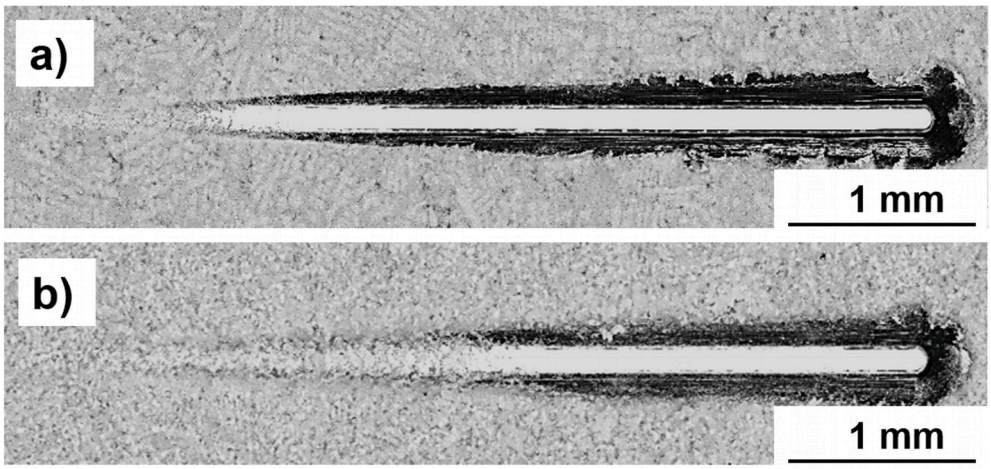

Fig. 11. Scratch test of MAO coatings: a) Test 5 sample and b) Test 8 sample (load 1–50 N, distance 50 mm).

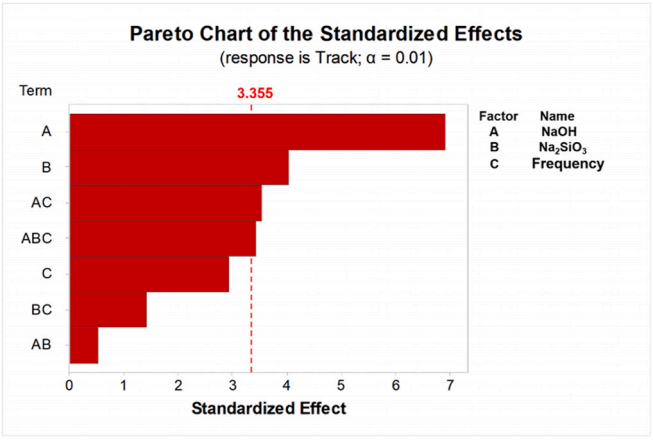

Fig. 12. Pareto chart of the standardised effect (α = 0.01).

formation of abrasive particles.

3.5. DOE analysis

Full factor analysis was used to systematically monitor the effects of selected main factors on the abrasion resistance of the MAO coatings. The statistically significant effect of the chosen parameters was evaluated using a Pareto diagram, which allows to graphically display the absolute value of the effect of individual factors or their combinations [36]. Fig. 12 shows the standardised effects for each factor, with the statistical significance denoted by the red reflection line (3.355). The most significant statistical effect on the abrasion resistance of MAO layers was confirmed for the NaOH content, the limiting contents of which were chosen concerning the micro-arc discharge (250–300 V) and the solubility of the layer. Higher contents (>9 g/l) led to the dissolution of the emerging MAO layer, which was observed on increasing current when the cut-offs were set. Another factor involving the Na_2SiO_3 content was statistically less significant. The effect of source frequency was not evaluated as a statistically significant factor in relation to the abrasion

Table 5
Corrosion resistance of MAO coatings.

Sample	E_{corr} (V)	I_{corr} (nA/cm^2)	R_p (MΩ·cm^2)	Corrosion rate (nm/year)
Substrate	−0.716	$5.500 \cdot 10^3$	0.00420	$59.910 \cdot 10^3$
Test 1	−0.176	$0.983 \cdot 10^3$	0.03801	$10.710 \cdot 10^3$
Test 2	−0.621	$0.033 \cdot 10^3$	1.23	368.8
Test 3	−0.629	5.548	4.82	60.42
Test 4	−0.143	29.497	1.66	321.2
Test 5	−0.668	0.300	41.39	3.266
Test 6	−0.670	4.576	8.48	49.83
Test 7	−0.653	4.051	8.71	44.11
Test 8	−0.796	2.433	21.62	26.50

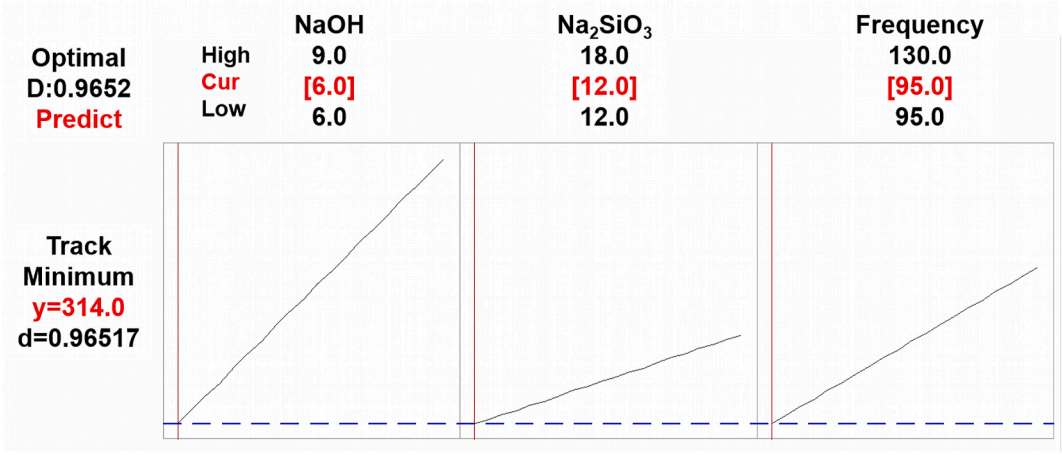

Fig. 13. Optimisation plot.

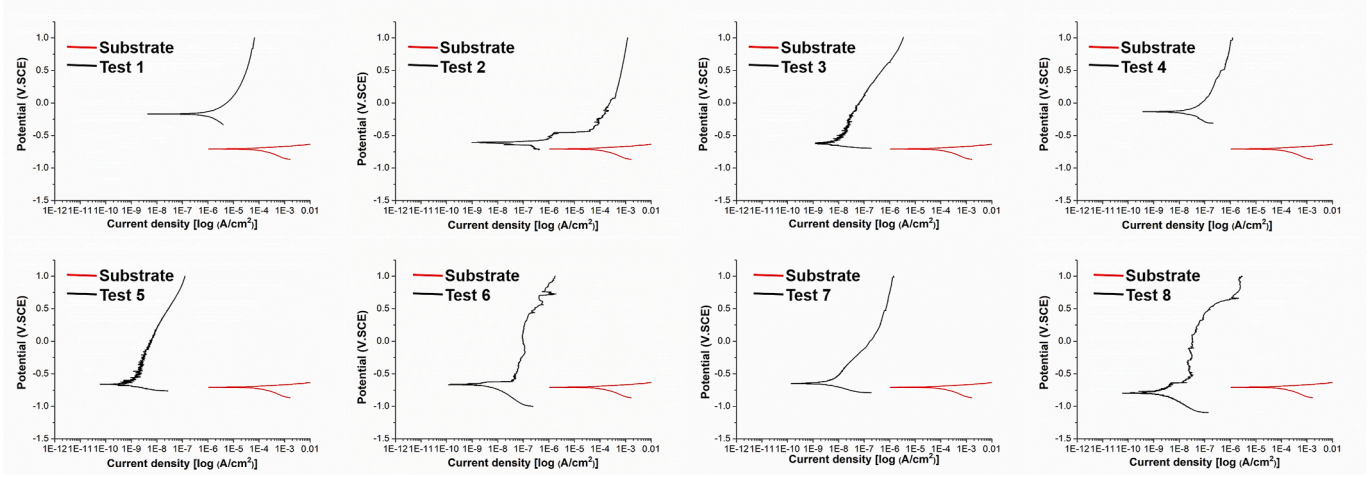

Fig. 14. Potentiodynamic curves of MAO coatings.

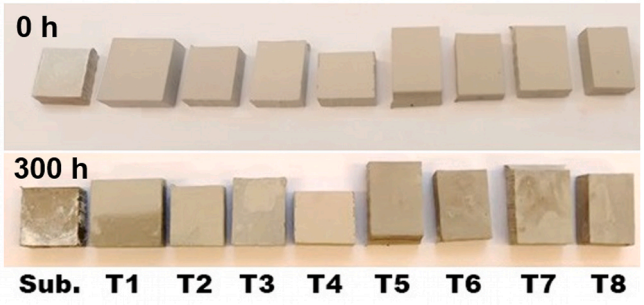

Fig. 15. Results of salt spray tests after 300 h.

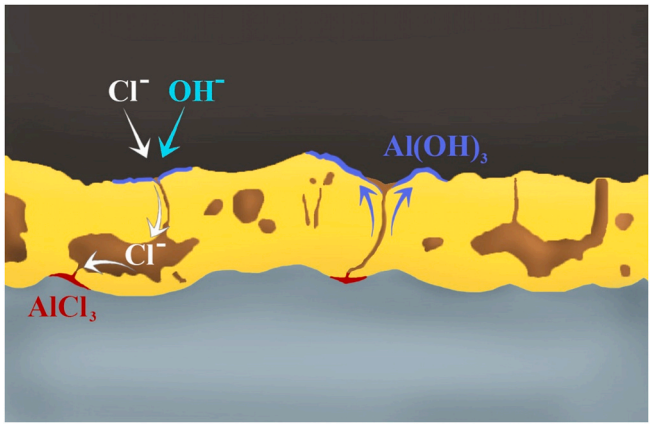

Fig. 16. Description and analysis of the formation of corrosion products, (a) corrosion mechanism, (b) SEM image of corrosion products, (c), (d) XPS spectrum Al 2p, O 1s.

resistance of MAO layers. Combinations of factors involving all three factors and/or combinations of NaOH with frequency were evaluated as less significant.

The combinations of individual factor optimal levels were evaluated from the perspective of DOE goal setting based on the minimum track width from the abrasion resistance evaluation results. The results of the optimised factor values are shown in red in Fig. 13. The recommended setting value for these factors is 96.52%. The resulting values correspond to Test 5 (Table 3) and are in good agreement with the results and the nature of the surface topography (Fig. 4). The significance of the factors, especially the concentration of ions in solution, affected the resulting surface quality in terms of the characteristic MAO defects present. The DOE test results have shown that this aspect has a direct influence on achieving the optimum MAO process parameters to achieve the desired tribological properties of the surfaces.

The multiple regression function (Eq. (6)) describes the dependence of the track width and the main observed factors (NaOH, Na_2SiO_3, frequency). The coefficient of multiple correlation (R-sq) and the adjusted coefficient of multiple correlation (R-sq(adj)) were used to evaluate the accuracy of the mathematical model. The determined values of R-sq = 92.54% and R-sq(adj) = 86.00% using Minitab® 17 software indicate sufficient accuracy of the model used. The highest statistical significance – in terms of the mathematical model used – can be confirmed for the NaOH factor.

$$\text{Track} = 5431 - 828\cdot\text{NaOH} - 502\cdot Na_2SiO_3 - 52.8\cdot\text{Frequency} + 76.2\cdot\text{NaOH}\cdot Na_2SiO_3 + 8.26\cdot\text{NaOH}\cdot\text{Frequency} + 4.77\cdot Na_2SiO_3\cdot\text{Frequency} - 0.694\cdot\text{NaOH}\cdot Na_2SiO_3\cdot\text{Frequency} \quad (6)$$

3.6. Corrosion behaviour

The corrosion resistance of MAO coatings in 3.5 wt % NaCl solution was described using the potentiodynamic polarisation curves shown in Fig. 14. Using Tafel guidelines, the values of corrosion potential (E_{corr}), corrosion current density (I_{corr}), polarisation resistance (R_p), and corrosion rate were calculated. The inhomogeneity of the coatings and the presence of defects associated with the MAO process (cracks, pores) affect the resulting electrochemical measurements. The polarisation curves shown in Fig. 14 and the resulting values shown in Table 5 thus directly demonstrate the influence of the defects present on the resulting corrosion resistance. The shift of the individual test curves to lower current density values shows the influence of MAO coatings on corrosion resistance. At the same time, an increase in polarisation resistance values and a decrease in corrosion rate can be observed, which is particularly evident in Test 5. The density and pore size play a key role in terms of corrosion resistance of MAO coatings due to the penetration of Cl^- and OH^- into the MAO coatings and the compactness of the internal MAO coating layer [37]. Tests with higher Na_2SiO_3 and NaOH content did not show increased corrosion resistance of MAO coatings. This fact is probably related to the defects present in MAO coatings due to the conduction of the discharge at its higher intensity. According to Yang et al. [38], increased Na_2SiO_3 contents lead to decreased corrosion resistance. On the contrary, the most corrosion-resistant MAO layer was confirmed in Test 5 with the lowest NaOH and Na_2SiO_3 contents.

The salt spray test results over time show the corrosion resistance of the prepared MAO layers for 300 h. On the surface of the MAO layers (Fig. 15) of the tests T1, T2, T3, T6, T7, and T8, locally porous corrosion products were observed. On the other hand, no corrosion products were observed on the MAO surfaces of samples T4 and T5 (Fig. 15), and can be considered satisfactory from the point of view of the test results. The

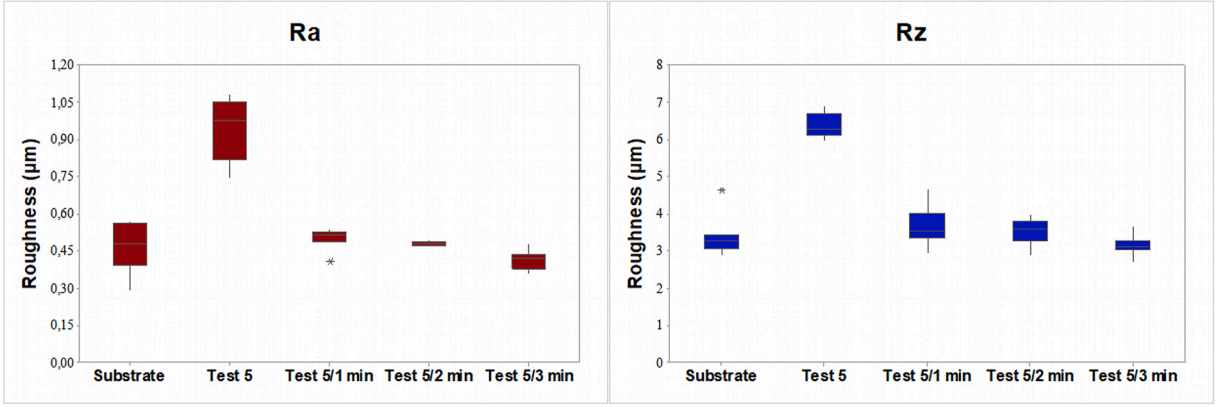

Fig. 17. Surface roughness of MAO coatings after aero-lap polishing.

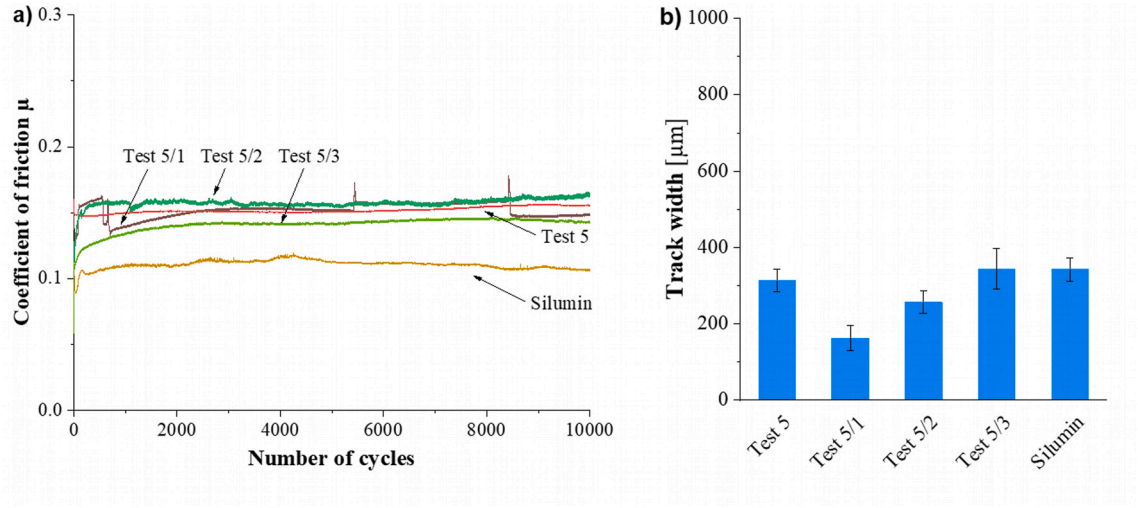

Fig. 18. Comparison of a) the friction coefficients and b) the wear tracks of the MAO layers Test 5 (untreated) and Test 5/1, Test 5/2, Test 5/3 (polished 1, 2, 3 min). Polished silumin was used as a reference.

Table 6
Chemical analysis of surfaces after polishing.

Test	wt. %		
	O	Al	Si
5/1 min	37.64 ± 0.28	48.96 ± 0.24	13.40 ± 0.14
5/2 min	37.86 ± 0.33	48.91 ± 0.28	13.23 ± 0.16
5/3 min	39.18 ± 0.32	50.34 ± 0.28	10.49 ± 0.14

presence of pitting corrosion was not demonstrated on the evaluated surfaces, probably due to the specified exposure time and corrosion resistance of the MAO layers. A description of the corrosion product formation mechanism and its representation is given in Fig. 16.

The presence and amount of corrosion products formed are determined by the amount and size of the present MAO coating defects. The formation of corrosion products occurs after hydrolysis of free Al^{3+} (Eq. (2)) ions at local pH change [39]. The surfaces of MAO coatings are covered with an amorphous passivating corrosion-resistant hydroxide layer (Eq. (7)) to form stable Al_2O_3 (Eq. (8)) corrosion products [40]. When Cl^- ions react with the passivation layer and subsequently penetrate the layer, depending on the amount and size of defects present, Cl^- can react with the substrate to form soluble products (Eq. (9)) [41].

$$Al^{3+} + 3OH^- \rightarrow Al(OH)_3 \quad (7)$$

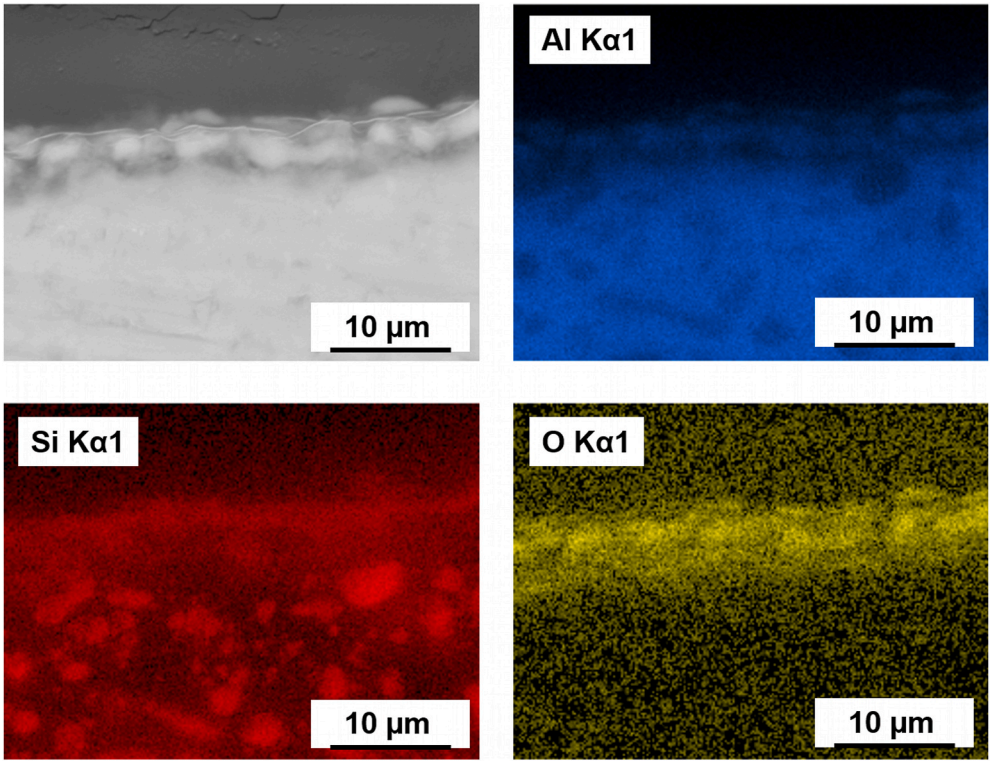

Fig. 19. EDX mapping of Test 5/1 coating after aero-lap polishing.

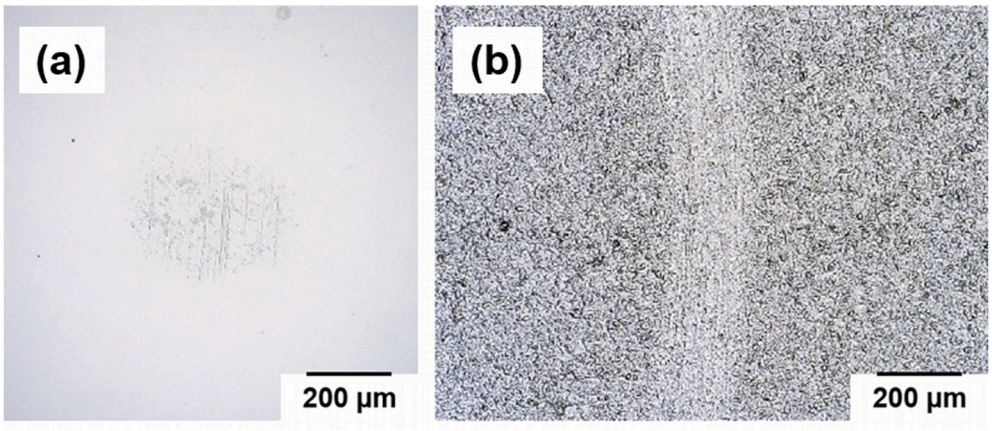

Fig. 20. The wear of the Al_2O_3 ball (a) and the wear track (b) of Test 5/1 sample.

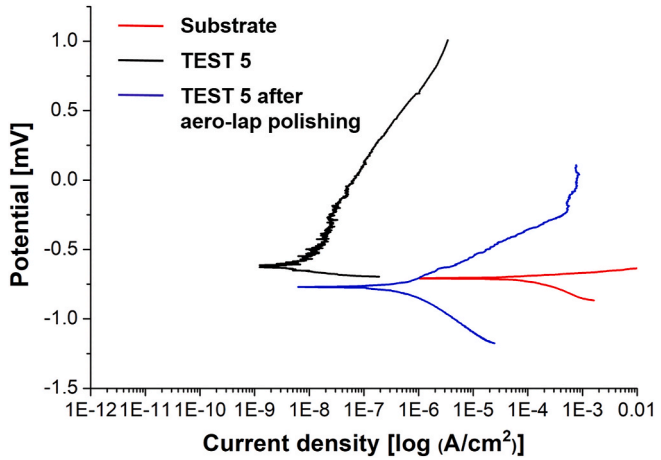

Fig. 21. Potentiodynamic curves of MAO coatings after aero-lap polishing.

$$2Al(OH)_3 \rightarrow Al_2O_3 + 3H_2O \quad (8)$$

$$Al^{3+} + 3Cl^- \rightarrow AlCl_3 \quad (9)$$

Fig. 16 presents the XPS spectrum of Test 7 after corrosion for elements O and Al. The results for the binding energies of elements O (530.2 eV) and Al (74.4 eV) confirm that there was a shift to lower energies of about 1 eV after corrosion, corresponding to the presence of the stable corrosion product Al_2O_3 (Eq. (8)). The presence of OH^- groups were not confirmed.

3.7. Final surface treatment to improve tribological properties

To be able to compare the friction coefficient courses and wear track width with the reference sample of silumin, the surface roughness of the Test 5 layer was treated by aero-lap polishing. Three types of surfaces were prepared by polishing for 1, 2 and 3 min (Test 5/1, Test 5/2 and Test 5/3). The aim was to create a surface roughness (Fig. 17) comparable to that of the reference silumin. At the same time, it was necessary to choose enough short polishing times so that the MAO layer remained thick enough on the surface of the samples.

Fig. 18a shows the course of the friction coefficients of the Test 5 sample in the untreated state and after polishing. Test 5/1 and 5/2 samples had a similar course to the untreated Test 5 samples. Only the Test 5/1 sample showed an unstable course of the initial phase. On the other hand, the Test 5/3 sample showed a stable course of the friction coefficient, which was closer to the friction coefficient of the silumin. This could indicate that the polishing time of 3 min is already too long, and that a substantial part of the MAO layer was removed. Similarly, if compare the wear track widths of the polished samples Test 5/2, Test 5/3 and silumin (Fig. 18b) are compared, approximately the same track widths are observed. The only exception was the Test 5/1 sample, where the wear track decrease indicated best the wear behaviour: Compared to silumin, this decrease was almost double.

The results of the chemical analysis of the coatings after polishing confirm the reduction in Si (Table 6) content to the values of the substrate, which confirms the removal of the MAO coating after 3 min. This corresponds to the decrease in the thickness of the MAO layer, where after only 1 min of surface polishing of the Test 5 sample, its thickness decreases from 9.2 ± 0.7 µm to 3.1 ± 0.6 µm.

Based on the cross-section and feature mapping performed (Fig. 19), it can be concluded that the use of the aero-lap polishing technique allows the removal of the outer porous layer, thus eliminating the increased irregularities associated with the craters and pores present on the surface of the porous outer layer. Fig. 19 shows a uniform MAO coating with roughness parameters R_a, R_z, which corresponds to the quality of the substrate surface. In addition to the presence of Al–Si–O in the polished surface layer, the presence of α(Al)+Si eutectic on the evaluated cross-sectional area is evident.

Fig. 20a confirms that the MAO coating wear after the aero-lap polishing is slightly abrasive and shows more abrasion resistance compared to Test 5 without polishing (Fig. 10a). It can also be concluded that the removal of the outer layer led to an increase in the abrasion resistance of the MAO layer of Test 5 compared to Test 5 without polishing and to the polished substrate (Fig. 20b). If the surface roughness is created on the Test 5 sample as on the silumin and not a substantial part of the MAO layer is removed, this modification clearly shows the best abrasion resistance of all compared samples, including silumin.

The resulting values of corrosion parameters show that after removal of the outer surface layer, there was a significant deterioration in their R_p (0.075 MΩ·cm^2), E_{corr} (−777.2 mV), I_{corr} (0.583.10^3 nA cm^{-2}), corrosion rate (16.839.10^3 nm/year) compared to MAO coating of Test 5 and substrate (Table 5). At the same time, the corrosion resistance of the treated layer is still better than that of silumin (Fig. 21). Besides, the application of aero-lap polishing showed that the removal of the outer layer leads to a decrease in the corrosion resistance of the MAO coating while improving the tribological properties. This fact confirms that the effect of an outer porous layer with higher silicon content [42] is associated with the higher corrosion resistance of MAO coating.

4. Conclusions

Ceramic layers with optimal tribological properties were prepared by MAO process using DOE technique at 500 V applied voltage and 60 min process time. The effect of individual factors on the tribological and

corrosion properties of the layers was investigated in a full factorial design. The uniform ceramic coating was prepared using a combination of the lowest NaOH (6 g/l) and Na_2SiO_3 (12 g/l) content with the smallest layer thickness. The most NaOH content was found to have the most significant statistical effect on the abrasion resistance of the ceramic coatings. The optimum values determined by DOE analysis were confirmed for the parameters of Test 5. The average values of the friction coefficients of the Test 1–8 samples were around 0.15 at steady state, i.e. slightly higher than the friction coefficient of 0.1 for polished silumin. The abrasion evaluated by the width wear track was the smallest of all the samples for the Test 5 sample. The ceramic layers of Test 5 also exhibited the best corrosion resistance, both from the spray test results and the potentiodynamic curve parameters evaluated. The abrasion of the outer layer using aero-lap polishing allowed reaching a comparable coefficient of friction to the polished substrate, and the width of the friction track was almost half that of the polished substrate. For these reasons, this combination of methods appears to be a suitable tool for preparing functional ceramic layers on cast AlSi10Mg for selected engine parts.

Declaration of competing interest

The authors declare that they have no known competing financial interests or personal relationships that could have appeared to influence the work reported in this paper.

Acknowledgements

The study was conducted with financial support from Ministry of Education, Youth and Sport of the Czech Republic SP2022/31 (Preparation and characterisation of advanced materials).

References

[1] G. Timmermans, L. Froyen, Fretting wear behaviour of hypereutectic P/M Al-Si in oil environment, Wear 230 (1999) 105–117, https://doi.org/10.1016/S0043-1648(98)00336-6.
[2] H.R. Ammar, A.M. Samuel, F.H. Samuel, Porosity and the fatigue behavior of hypoeutectic and hypereutectic aluminum–silicon casting alloys, Int. J. Fatig. 30 (2008) 1024–1035, https://doi.org/10.1016/j.ijfatigue.2007.08.012.
[3] M. Javidani, D. Larouche, Application of cast Al-Si alloys in internal combustion engine components, Int. Mater. Rev. 59 (2014) 132–158, https://doi.org/10.1179/1743280413Y.0000000027.
[4] Ch Vargel, Corrosion of Aluminium, second ed., 2020, p. 852, https://doi.org/10.1016/C2012-0-02741-X, 978-0-08-099925-8.
[5] S.H. Mohitfar, S. Mahdavi, M. Etminanfar, J. Khalil-Allafi, Characteristics and tribological behavior of the hard anodised 6061-T6 Al alloy, J. Alloys Compd. 842 (2020), 155988, https://doi.org/10.1016/j.jallcom.2020.155988.
[6] B. Rajasekaran, S.G.S. Raman, L.R. Krishna, S.V. Joshi, G. Sundararajan, Influence of microarc oxidation and hard anodizing on plain fatigue and fretting fatigue behaviour of Al–Mg–Si alloy, Surf. Coat. Technol. 202 (2008) 1462–1469, https://doi.org/10.1016/j.surfcoat.2007.06.058.
[7] M.P. Martínez-Viademonte, S.T. Abrahami, T. Hack, M. Burchardt, H. Terryn, A Review on Anodizing of Aerospace Aluminum Alloys for Corrosion Protection Coatings 10 (2020) 1106, https://doi.org/10.3390/coatings10111106.
[8] P. Poza, M.A. Garrido-Maneiro, Cold-sprayed coatings: microstructure, mechanical properties, and wear behaviour, Prog. Mater. Sci. 123 (2022), 100839, https://doi.org/10.1016/j.pmatsci.2021.100839.
[9] J.A. Picas, A. Forn, R. Rilla, E. Martín, HVOF thermal sprayed coatings on aluminium alloys and aluminium matrix composites, Surf. Coat. Technol. 200 (2005) 1178–1181, https://doi.org/10.1016/j.surfcoat.2005.02.124.
[10] J. He, Q.Z. Cai, H.H. Luo, L. Yu, B.K. Wei, Influence of silicon on growth process of plasma electrolytic oxidation rating on Al-Si alloy, J. Alloys Compd. 471 (2009) 395–399, https://doi.org/10.1016/j.jallcom.2008.03.114.
[11] I.J. Hwang, D.Y. Hwang, Y.M. Kim, B. Yoo, D.H. Shin, Formation of uniform passive oxide layers on high Si content Al alloy by plasma electrolytic oxidation, J. Alloys Compd. 504 (2010) S527–S530, https://doi.org/10.1016/j.jallcom.2010.02.074.
[12] P. Fernández-López, S.A. Alves, A. López-Ortega, J.T. San José-Lombera, R. Bayón, High performance tribological coatings on a secondary cast Al–Si alloy generated by Plasma Electrolytic Oxidation, Ceram. Int. 47 (2021) 31238–31250, https://doi.org/10.1016/j.ceramint.2021.07.300.
[13] M. Mohedano, E. Matykina, R. Arrabal, B. Mingo, A. Pardo, PEO of pre-sanodised Al–Si alloys: corrosion properties and influence of sealings, Appl. Surf. Sci. 346 (2015), https://doi.org/10.1016/j.apsusc.2015.03.206, 57-56.
[14] M. Kaseem, S. Fatimah, N. Nashrah, Y.G. Ko, Recent progress in surface modification of metals coated by plasma electrolytic oxidation: principle, structure, and performance, Prog. Mater. Sci. 117 (2021), 100735, https://doi.org/10.1016/j.pmatsci.2020.100735.
[15] J. Li, H. Cai, X. Xue, B. Jiang, The outward–inward growth behavior of microarc oxidation coatings in phosphate and silicate solution, Mater. Lett. 64 (2010) 2102–2104, https://doi.org/10.1016/j.matlet.2010.06.053.
[16] W. Xue, X. Shi, M. Hua, Y. Li, Preparation of anti-corrosion films by microarc oxidation on an Al–Si alloy, Appl. Surf. Sci. 253 (2007) 6118–6124, https://doi.org/10.1016/j.apsusc.2007.01.018.
[17] W. Xue, Ch Wang, Y. Li, R. Chen, T. Zhang, Analyses of microarc oxidation coatings formed on Si containing cast aluminum alloy in silicate solution, ISIJ Int. 42 (2002) 1273–1277, https://doi.org/10.2355/isijinternational.42.1273.
[18] F. Xu, Y. Xia, G. Li, The mechanism of PEO process on Al–Si alloys with the bulk primary silicon, Appl. Surf. Sci. 255 (2009) 9531–9538, https://doi.org/10.1016/j.apsusc.2009.07.090.
[19] A.L. Yerokhin, X. Nie, A. Leyland, A. Matthews, S.J. Dowey, Plasma electrolysis for surface engineering, Surf. Coat. Technol. 122 (1999) 73–93, https://doi.org/10.1016/S0257-8972(99)00441-7.
[20] Z. Wang, L. Wu, Y. Qi, W. Cai, Z. Jiang, Self-lubricating Al_2O_3/PTFE composite coating formation on surface of aluminium alloy, Surf. Coat. Technol. 204 (2010) 3315–3318, https://doi.org/10.1016/j.surfcoat.2010.03.049.
[21] K.J. Ma, M.M.S. Al Bosta, W.T. Wu, Preparation of self-lubricating composite coatings through a micro-arc plasma oxidation with graphite in electrolyte solution, Surf. Coat. Technol. 259 (2014) 318–324, https://doi.org/10.1016/j.surfcoat.2014.03.004.
[22] M. Aliofkhazraei, A.S. Rouhaghdam, T. Shahrabi, Abrasive wear behaviour of Si_3N_4/TiO_2 nanocomposite coatings fabricated by plasma electrolytic oxidation, Surf. Coat. Technol. 205 (2010) S41–S46, https://doi.org/10.1016/j.surfcoat.2010.03.052.
[23] M. Mu, J. Liang, X. Zhou, Q. Xiao One-step preparation of TiO_2/MoS_2 composite coating on Ti6Al4V alloy by plasma electrolytic oxidation and its tribological properties, Surf. Coat. Technol. 214 (2013) 124–130, https://doi.org/10.1016/j.surfcoat.2012.10.079.
[24] B. Gunter, D. Coleman, A DOE Handbook:A Simple Approach to Basic Statistical Design of Experiments, 2014, p. 118, 13: 9781497511903.
[25] M.M.S. Al Bosta, K.J. Ma, H.H. Chien, The effect of MAO processing time on surface properties and low temperature infrared emissivity of ceramic coating on aluminium 6061 alloy Infrared, Phys. Technol. 60 (2013) 323–334, https://doi.org/10.1016/j.infrared.2013.06.006.
[26] R.H.U. Khan, A. Yerokhin, X. Li, H. Dong, A. Matthews, Surface characterisation of DC plasma electrolytic oxidation treated 6082 aluminium alloy: effect of current density and electrolyte concentration, Surf. Coat. Technol. 205 (2010) 1679–1688, https://doi.org/10.1016/j.surfcoat.2010.04.052.
[27] R.F. Zhang, S.F. Zhang, J.H. Xiang, L.H. Zhang, Y.Q. Zhang, S.B. Guo, Influence of sodium silicate concentration on properties of micro arc oxidation coatings formed on AZ91HP magnesium alloys, Surf. Coat. Technol. 206 (2012) 5072–5079, https://doi.org/10.1016/j.surfcoat.2012.06.018.
[28] A. Polat, M. Makaraci, M. Usta, Influence of sodium silicate concentration on structural and tribological properties of microarc oxidation coatings on 2017A aluminum alloy substrate, J. Alloys Compd. 504 (2010) 519–526, https://doi.org/10.1016/j.jallcom.2010.06.008.
[29] G. Sundararajan, L.R. Krishna, Mechanisms underlying the formation of thick alumina coatings through the MAO coating technology, Surf. Coat. Technol. 167 (2003) 269–277, https://doi.org/10.1016/S0257-8972(02)00918-0.
[30] W. Ch Gu, G.H. Lv, Ch Huan, Ch G. Liang, F.W. Ran, Z.G. Ling, Y.S. Ze, Investigation of morphology and composition of plasma electrolytic oxidation coatings in systems of Na_2SiO_3–NaOH and $(NaPO_3)_6$–NaOH, J. Mater. Process. Technol. 182 (2007) 28–33, https://doi.org/10.1016/j.jmatprotec.2006.07.002.
[31] L.O. Snizhko, A.L. Yerokhin, A. Pilkington, N.L. Gurevina, D.O. Misnyankin, A. Leyland, A. Matthews, Anodic processes in plasma electrolytic oxidation of aluminium in alkaline solutions Electrochim, Acta 49 (2004) 2085–2095, https://doi.org/10.1016/j.electacta.2003.11.027.
[32] S. Wang, X. Liu, X. Yin, N. Du, Influence of electrolyte components on the microstructure and growth mechanism of plasma electrolytic oxidation coatings on 1060 aluminum alloy, Surf. Coat. Technol. 381 (2020), 125214, https://doi.org/10.1016/j.surfcoat.2019.125214.
[33] K. Li, W. Li, G. Zhang, W. Zhu, F. Zheng, D. Zhang, M. Wang, Effects of Si phase refinement on the plasma electrolytic oxidation of eutectic Al-Si alloy, J. Alloys Compd. 790 (2019) 650–656, https://doi.org/10.1016/j.jallcom.2019.03.217.
[34] S. Wannaparhun, S. Seal, V. Desai, Surface chemistry of Nextel-720, alumina and Nextel-720/alumina ceramic matrix composite (CMC) using XPS–A tool for nano-spectroscopy, Appl. Surf. Sci. 185 (2002) 183–196, https://doi.org/10.1016/S0169-4332(01)00594-3.
[35] Handbook of Photoelectron Spectroscopy, Jill Chastain Perkin-Elmer Corporation, Minesota, USA, 1992.
[36] D.C. Montgomery, Design and Analysis of Experiments, vol. 656, John Wiley & Sons, Inc., USA, 2009. ISBN 978-0-470-12866-4.
[37] K. Zhang, S. Yu, Preparation of wear and corrosion resistant micro-arc oxidation coating on 7N01 aluminum alloy, Surf. Coat. Technol. 388 (2020), 125453, https://doi.org/10.1016/j.surfcoat.2020.125453.
[38] Z. Yang, X.Z. Zhang, Y.K. Wu, G.R. Wu, D.D. Wang, X.T. Liu, H.P. Han, Y. Su, D. J. Shen, The correlation between the $Na_2SiO_3{\cdot}9H_2O$ concentrations and the characteristics of plasma electrolytic oxidation ceramic coatings, Ceram. Int. 45 (2019) 19388–19394, https://doi.org/10.1016/j.ceramint.2019.06.191.

[39] X. Huang, L. Yu, Y. Dong, Corrosion resistance of a novel ceria doped aluminum phosphate ceramic coating on cast Al-Si alloy by steam-assisted curing Corros, Science 182 (2021), 109256, https://doi.org/10.1016/j.corsci.2021.109256.
[40] C. Peng, Y.W. Liu, M.X. Guo, T.Z. Gu, Ch Wang, Z.Y. Wang, Ch Sun, Corrosion and pitting behaviour of pure aluminium 1060 exposed to Nansha Islands tropical marine atmosphere, Trans. Nonferrous Metals Soc. China 32 (2022) 448–460, https://doi.org/10.1016/S1003-6326(22)65806-0.
[41] K. Xi, H. Wu, Ch Zhou, Z. Qi, K. Yang, R.K.Y. Fu, S. Xiao, G. Wu, K. Ding, G. Chen, P.K. Chu, Improved corrosion and wear resistance of micro-arc oxidation coatings on the 2024 aluminum alloy by incorporation of quasi-two-dimensional sericite microplates Appl, Surf. Sci. 585 (2022), 152693, https://doi.org/10.1016/j.apsusc.2022.152693.
[42] R. Gabor, M. Doubkova, S. Gorosova, K. Malanik, M. Vandrovcova, L. Cvrcek, K. Drobikova, K. Mamulova Kutlakova, L. Bacakova, Preparation of highly wettable coatings on Ti–6Al–4V ELI alloy for traumatological implants using micro-arc oxidation in an alkaline electrolyte, Sci. Rep. 10 (2020) 19780, https://doi.org/10.1038/s41598-020-76448-w.